

Ultrashort chirped pulse evolution in silicon photonic nanowires

Jiali Liao (廖家莉)^{1*}, Matthew Marko (马修.马克)^{2,3}, Hui Jia (贾辉)¹,
Wenchao Sun (孙文超)¹, Ju Liu (刘菊)¹, Yizhou Tan (谭一舟)⁴,
Jiankun Yang (杨建坤)¹, Xiaochun Wang (王潇春)¹, Yuanda Zhang (张远达)¹,
Wusheng Tang (唐武胜)¹, Xiujian Li (李修建)¹, and Chee Wei Wong (黄智维)²

¹College of Science, National University of Defense Technology, Changsha, Hunan 410073, China

²Optical Nanostructures Laboratory, Columbia University, New York, NY 10027, USA

³Navy Air Warfare Center Aircraft Division (NAWCAD), Joint Base McGuire Dix Lakehurst, Lakehurst NJ 08733, USA

⁴College of Mechatronics and Automation, National University of Defense Technology, Changsha, Hunan 410073, China

*Corresponding author: nancy19860803@163.com

Received August 05, 2013; accepted October 09, 2013; posted online March 20, 2014

We investigate the ultrafast nonlinear phenomena of picosecond chirped non-ideal hyperbolic secant pulse evolution in silicon photonic nanowire waveguides with sum frequency generation cross-correlation frequency-resolved optical gating and nonlinear Schrödinger equation modeling. Pulse broadening and spectral blue shifts are observed experimentally, and they show remarkable agreements with numerical predictions. Nonlinear losses dominate the pulse broadening and limit the spectral bandwidth broadening induced by self-phase modulation. The initial chirp results in noticeable bandwidth compression and aggravation of blue shifts in the presence of nonlinear losses, whereas it plays a negligible role in the output pulse temporal intensity distribution.

OCIS codes: 190.7110, 320.5390, 320.1590.

doi: 10.3788/COL201412.S11905.

Silicon waveguides have been attracting increasing attention for photonic-integrated circuits due to the development of fabrication technology and compatibility with mature CMOS technologies^[1-4]. Optical soliton dynamics in silicon nanowires has been extensively investigated, including the formation of fundamental soliton and high-order soliton effects^[5-8], with potential applications ranging from optical amplification^[9], pulse compressing^[10,11], supercontinuum generation^[11-13] to passively mode-locked lasers^[14]. The propagation of temporal solitons is affected by the inherent dispersion and nonlinear properties of silicon waveguides^[1] along with linear losses that arise due to disorder scattering^[3]. In addition, the initial chirp and shape distortion are inevitable and play a noticeable role in the pulse evolution^[15], which should be investigated further.

We have constructed a high-sensitive cross-correlation frequency-resolved optical gating (XFROG) to investigate the chirped pulse dynamics through the SPNW, with remarkable agreements with the experimental observations. Impacts of losses by both linear and nonlinear mechanisms on the pulse evolution are described in detail. Furthermore, the effects of initial chirp and non-ideal hyperbolic secant shape on pulse dynamics are investigated, which is significant for its practical

application in photonic signal processing and communication systems.

Figure 1(a) represents the scanning electron micrograph and schematic cross-section of the silicon waveguide measured in this study. It is a single-mode SPNW with cross-section $A_0 = 450 \times 250 \text{ nm}^2$ and length $L = 4 \text{ mm}$, a buried oxide thickness of $3 \mu\text{m}$, and covered by a $3\text{-}\mu\text{m}$ oxide layer. Oxide-cladded inverted tapered couplers are adopted to improve the input-output coupling. The coupling into and output from the SPNW were in free space in order to minimize the influence of fiber's nonlinearities, with typical total input-chip-output coupling loss of about 10 dB.

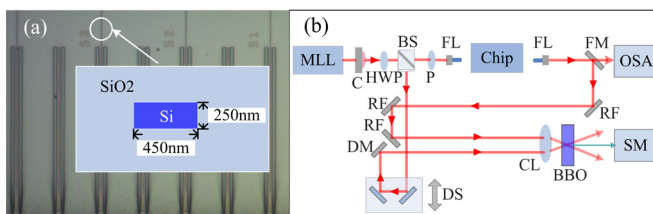


Fig. 1. (a) Scanning electron micrograph and schematic cross-section of the chip-scale silicon waveguide examined in this study. (b) Experimental setup with SFG-XFROG. MLL, mode-locked fiber laser; HWP, half-wave plate; C, optical collimator; BS, beam splitter; P, polarizer; FL, focus lens; FM, flip mirror; OSA, optical spectrum analyzer; RF, reflector; DM, D-shape mirror; DS, delay stage; CL, bi-convex lens; BBO, crystal barium borate crystal; SM, spectrometer with a liquid nitrogen-cooled CCD detector.

The experimental setup with sum frequency generation cross-correlation frequency-resolved optical gating (SFG-XFROG) is shown in Fig. 1(b), in which a high-sensitive grating spectrometer, i.e., Horiba JY 1000M-II with BIDD CCD detector and a piece of BBO with 1-mm thickness to detect ultra-low-pulse energy down to 1.0 fJ. A mode-locked fiber laser (PolarOnyx Saturn series) emitting 2.3 ps pulses train at a 39.1-MHz repetition rate was utilized, with tunable center wavelength range from 1535 to 1560 nm and maximum pulse energy up to approximately 600 pJ at 1535 nm. A half-wave plate and linear polarizer pair controls the pulse energy and ensures that transverse-electric polarization is coupled with the waveguide. In addition, the validity of the experiments is enhanced by comparing the spectra measured by optical spectrum analyzer with the retrieved spectra.

Two-dimensional XFROG-retrieved traces of input pulses and output pulses at waveguide output at 533 μW and 3230 μW input power are illustrated in Figs. 2(a)–(c). The retrieved XFROG error, in the 2D phase-retrieval solution and convergence, is determined to be less than 0.5% for each of the datasets reported here, which confirms the alignment of the setup. Furthermore, the XFROG trace has the advantage of unambiguous time direction compared with traditional FROG trace, which is necessary for pulse evolution analysis^[16].

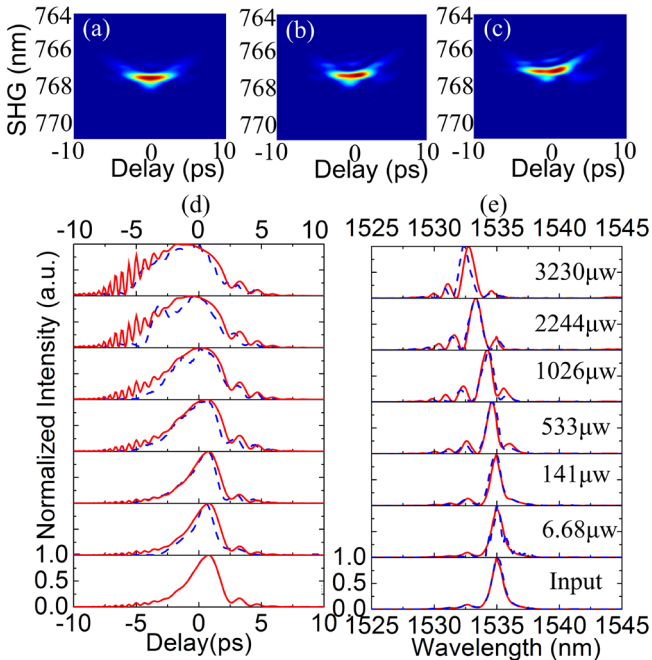


Fig. 2. Two-dimensional XFROG-retrieved traces for input pulses (a) and output pulses at 533 μW (b) and at 3230 μW (c) input power of 1535-nm central wavelength, with a retrieved error below 0.5%. Pulse shapes (d) and spectra (e) of input pulse and output pulses for increasing coupled power, wherein XFROG retrieved in blue dashed line, numerically predicted in red solid line. The label denotes the coupled power at the waveguide input.

We concurrently perform the NLSE modeling to investigate the pulse evolution, in which the initial pulse is from the XFROG measurement, which helps ensure the uniformity between the simulation conditions and experiment conditions. Main parameters in the simulations are group velocity dispersion coefficient $\beta_2 = -1.53\text{ps}^2/\text{m}$, calculated by the finite-differential time-domain algorithm^[17]; the linear loss $\alpha_l = 0.5\text{dB}/\text{mm}$; the nonlinear index $n_2 = 6 \times 10^{-18}\text{m}^2/\text{W}$ ^[18]; the two-photon absorption (TPA) coefficient $\beta_{\text{TPA}} = 11 \times 10^{-12}\text{m}/\text{W}$ ^[18]. Simulation results are illustrated in Figs. 2(d) and (e), comparing with the experimental results, which show remarkable agreements with each other, wherein the pulse exhibits increasing temporal broadening and blue shift with an increase in coupled optical power.

We illustrate the effects of the initial chirp, non-ideal hyperbolic secant pulse shape and losses by linear and non-linear mechanisms on the pulse evolution in Fig. 3,

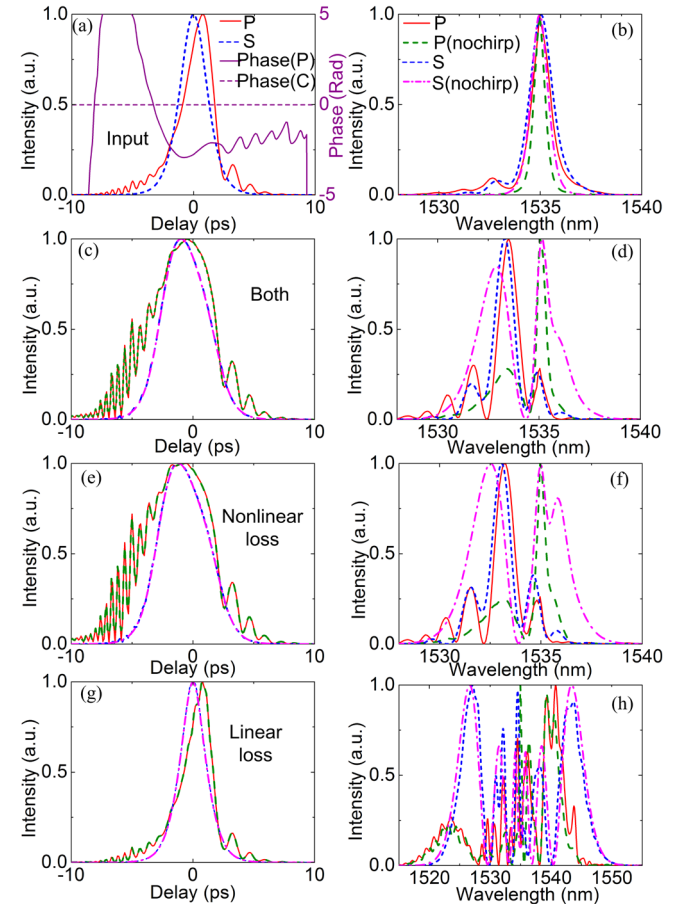


Fig. 3. Temporal pulse shapes and phase distributions (a) and spectra (b) of input pulses for the simulations. Output pulse shapes and spectra at 2000 μW input power; the conditions include two mechanism losses (c) and (d), including only nonlinear losses (e) and (f), and also only linear losses (g) and (h). Practical input cases are represented as solid red curve, practical input without chirp in olive-dashed curve, ideal hyperbolic secant with chirp in blue short-dashed curve and hyperbolic secant without chirp in magenta dash dot curve. Practical chirped phase in solid purple curve and constant phase without chirp is represented in dashed purple line.

on the basis of NLSE modeling. Figure 3(a) shows the temporal pulse shapes and phase distributions of input pulses. There are two types of input pulse shapes in the simulation, in which one is practical shape of experiments and the other is ideal hyperbolic secant. The two types of the pulse shapes are appended by either chirped phase or constant phase, respectively, composing four different input conditions. The chirped phase is same as that of experimental input and is quite slight, with only 0.08π standard deviation, while the constant phase is set at 0. The input spectra of aforementioned four conditions are shown in Fig. 3(b), in which there are obvious side small peaks and slight bandwidth broadening induced by the chirped phase.

Figures 3(c), (e) and (g) show the temporal output pulse shapes for four input conditions, considering two mechanism losses, nonlinear losses or linear losses. Nonlinear losses induced by TPA dominate the pulse broadening as a result of the pulse central peak region attenuation by the intensity-dependent absorption. On the other hand, the initial chirp plays a negligible role in the output pulse temporal intensity in all cases, as the GVD is relatively low. Furthermore, comparison of Fig. 3(c) with (e) showed that linear losses limit the extent of nonlinear pulse broadening by attenuating the pulse intensity to limit the intensity-dependent nonlinear absorption.

The spectra of output pulses are shown in Figs. 3(d), (f) and (h). The spectra exhibit an oscillatory structure, which is obtained from the SPM-induced frequency chirp, and the nonlinear losses alleviate the SPM-induced wavelength splitting significantly. A remarkable bandwidth broadening is induced by self-phase modulation (SPM)^[19] for all cases, whereas the nonlinear losses limit the spectral broadening, comparing Figs. 3(d) and (h), which shows that the scales of wavelength are different. Linear losses play a minor role in the output spectra, as compared between Figs. 3(d) and (f). On the other hand, we observe that the initial chirp results in noticeable bandwidth compression, in the presence of nonlinear losses, and also aggravates the blue shifts, though the free carrier dispersion induced by TPA dominates the blue shift^[19]. Effects of initial chirp can be neglected in the absence of nonlinear losses, as shown in Fig. 3(h). In addition, the non-ideal hyperbolic secant shape results in obvious spectral distortions; however, the distortions become slight when nonlinear losses and initial chirp are combined, as illustrated in Figs. 3(d) and (f) with red solid curves and blue short dashed curves.

In conclusion, demonstrate the evolution of chirped non-ideal hyperbolic pulses with XFROG and NLSE modeling. The phenomena examined by experiments

match remarkably with NLSE modeling predictions, with pulse broadening and spectral blue shifts. The nonlinear losses are dominated by TPA results in remarkable pulse broadening and limitation of SPM spectral broadening. At the same time, the linear losses not only attenuate the output power linearly, but also limit the extent of pulse broadening induced by nonlinear absorption. On the other hand, the initial chirp results in noticeable bandwidth compression, in the presence of nonlinear losses, and also aggravates the blue shifts. In addition, the spectral distortions induced by the non-ideal hyperbolic secant shape are weakened by the nonlinear losses and initial chirp combination.

This research was supported by the National Natural Science Foundation of China (NSFC) under Grant No. 61070040, 61108089, 61205087 and 61107005. We thank James F. McMillan and Jangjun Zheng for their help when performing some of the measurements in Optical Nanostructures Laboratory in Columbia University.

References

1. Q. Lin, O. J. Painter, and G. P. Agrawal, *Opt. Express* **15**, 16604 (2007).
2. D. Dai and J. E. Bowers, *Opt. Express* **19**, 10940 (2011).
3. M. A. Foster¹, A. C. Turner, M. Lipson, and A. L. Gaeta, *Opt. Express* **16**, 1300 (2008).
4. K. Liu, W. Xu, Z. Zhu, W. Ye, X. Yuan, and C. Zeng, *Opt. Lett.* **37**, 2826 (2012).
5. J. Zhang, Q. Lin, G. Piredda, R. W. Boyd, G. P. Agrawal, and P. M. Fauchet, *Opt. Express* **15**, 7682 (2007).
6. L. H. Yin, Q. Lin, and G. P. Agrawal, *Opt. Lett.* **31**, 1295 (2006).
7. S. C. V. Latas and M. F. S. Ferreira, *Opt. Lett.* **35**, 1071 (2010).
8. R. Hao, L. Li, R. Yang, Z. Li, and G. Zhou, *Chin. Opt. Lett.* **3**, 030136 (2005).
9. W. H. Renninger, A. Chong, and F. W. Wise, *Opt. Lett.* **33**, 3025 (2008).
10. X. Zeng, H. Guo, B. Zhou, and M. Bache, *Opt. Express* **20**, 27072 (2012).
11. M. A. Foster and A. L. Gaeta, *Opt. Express* **13**, 6848 (2005).
12. L. H. Yin, Q. Lin, and G. P. Agrawal, *Opt. Lett.* **32**, 391 (2007).
13. E. J. R. Kelleher, M. Erkintalo, and J. C. Travers, *Opt. Lett.* **37**, 5217 (2012).
14. P. Grelul and N. Akhmediev, *Nat. Photon.* **6**, 84 (2012).
15. L. M. Mandeng and C. Tchawoua, *J. Opt. Soc. Am. B* **30**, 1382 (2013).
16. W. Ding, A. V. Gorbach, W. J. Wadsworth, J. C. Knight, D. V. Skryabin, M. J. Strain, M. Sorel, and R. M. De La Rue, *Opt. Express* **18**, 26625 (2010).
17. N. Kejalakshmy, A. Agrawal, Y. Aden, D. M. H. Leung, B. M. A. Rahman, and K. T. V. Grattan, *Appl. Opt.* **49**, 3173 (2010).
18. A. D. Bristow, N. Rotenberg, and H. M. van Drielb, *Appl. Phys. Lett.* **90**, 191104 (2007).
19. L. H. Yin and G. P. Agrawal, *Opt. Lett.* **32**, 2031 (2007).